Full paper

Significantly reduced thermal conductivity and enhanced thermoelectric properties of single- and bi-layer graphene nanomeshes with sub-10 nm neck-width

Jinwoo Oh[a,b], Hoyeon Yoo[a,c], Jaeyoo Choi[a], Jeong Yun Kim[d], Dong Su Lee[e], Myung Jong Kim[e], Jong-Chan Lee[b], Woo Nyon Kim[c], Jeffrey C. Grossman[d], Jong Hyuk Park[a], Sang-Soo Lee[a], Heesuk Kim[a], Jeong Gon Son[a,*]

[a] Photo-Electronic Hybrids Research Center, Korea Institute of Science and Technology, Seoul 02792, Republic of Korea
[b] School of Chemical & Biological Engineering, Seoul National University, Seoul 08826, Republic of Korea
[c] Department of Chemical & Biological Engineering, Korea University, Seoul 02841, Republic of Korea
[d] Department of Materials Science & Engineering, Massachusetts Institute of Technology, Cambridge, MA 02139, USA
[e] Soft Innovative Materials Research Center, Korea Institute of Science and Technology, Wanju-gun, Jeollabuk-do 55324, Republic of Korea

ARTICLE INFO

ABSTRACT

When graphene is shrunk into ~10 nm scale graphene nanoribbons or nanomesh structures, it is expected that not only electrical properties but also thermal conductivity and thermoelectric property are significantly altered due to the quantum confinement effect and extrinsic phonon-edge scattering. Here, we fabricate large-area, sub-10 nm single- and bilayer graphene nanomeshes from block copolymer self-assembly and measure the thermal conductivity, thermoelectric and electrical transport properties to experimentally verify the effect of sub-10 nm quantum confinement, phonon-edge scattering and cross-plane coupling. Among the large variety of the samples, bilayer graphene nanomesh having 8 nm-neck width showed significantly low thermal conductivity down to ~78 W m^{-1} K^{-1}, which is the lowest thermal conductivity for suspended graphene nanostructures, and a high thermopower value of −520 μV K^{-1}, while it still shows the comparably high carrier mobility. Classical and quantum mechanical calculations successfully supported our nanomesh approach, which can achieve high thermoelectric properties based on the significantly reduced thermal conductivity and higher thermopower due to the confined geometry.

1. Introduction

Graphene, as an atomically thin 2-dimensional allotrope of carbon materials, exhibits exceptional properties, such as superior electrical and thermal conductivity, high transparency [1], intrinsic zero bandgap and semi-metallic nature. The modification of graphene structures including hydrogenation [2], doping [3] and patterning [4] can maintain their superior properties and simultaneously tailor or enhance specific properties for various applications. When graphene is modified into graphene nanoribbons (GNRs) or nanomeshes (GNMs), a noticeable bandgap is induced due to quantum confinement and a high on/off current ratio in field effect can be achieved [4–9]. Bilayer graphene structure also can derive the small bandgap because of an inversion symmetry breaking [10,11]. Several graphene nanostructure fabrication methods were suggested, including unzipping carbon nanotubes [8], nanowire etch masks [9] and e-beam lithography [4].

However, these methods only obtain a single-strand GNR or micron-size patterned graphene structures. Instead, a microphase-separated block copolymer (BCP) self-assembly [12–14] can be more suitable for large scale (over centimeter) production of 5–50 nm periodical GNMs [15–17] and GNR bundles [18–20].

Thermal conductivity of graphene [21–23] also has been recently and actively investigated after the first measurement of thermal conductivity from Balandin group in 2008 [24], because of unusual thermal transport behavior from the atomically thin 2D materials. The thermal conductivity of single layer graphene was measured extremely high over 3000 W m^{-1} K^{-1} [21,22], which is far above the bulk graphite limit. It mainly originated from the lattice vibration from strong covalent sp^2 bonding and long mean free path of phonon. Nanostructured defects which induce phonon-edge scattering and phonon spectra modification are known to significantly reduce and systematically control the thermal conductivity of low dimensional

materials including graphene. However, thermal transport in nanostructured or defected graphene has not fully understood and not yet been proven experimentally. Only limited thermal conductivity measurements have been reported such as isotopically defected graphene by ^{13}C atoms [25] and 45-nm-wide e-beam patterned GNRs on substrate [26].

The thermoelectric effect can be described as a temperature difference creates an electric potential. The thermoelectric efficiency is quantified by a figure of merit, given by $ZT = (S^2 \cdot \sigma) \cdot T / \kappa$, where S, σ, T, and κ are the Seebeck coefficient (thermopower), electrical conductivity, temperature, and thermal conductivity, respectively. In case of graphene, the notably high electrical conductivity can be a superior advantage; however, thermal conductivity is severely high. Furthermore, graphene intrinsically has a relatively low thermopower value less than $100\ \mu V\ K^{-1}$ due to the zero-bandgap nature [27]. Therefore, for a better thermoelectric efficiency, it is required to reduce the thermal conductivity and increase thermopower while maintaining the intrinsic high electrical conductivity [21–23]. Many computational researchers have suggested various graphene nanostructures in the range of 10 nm scale for significant enhancement of thermoelectric efficiency. This can be achieved in zigzag and armchair GNRs [28–30], GNMs [31–33] and graphene superlattice [34,35] with controlled number of graphene layers [36,37] by tuning band structures for superior thermopower and reducing thermal conductivity through the dominant phonon-edge scattering. However, no experimental results have been reported for nanostructured graphene. There was only a report on the enhancement of thermopower of a few-layer graphene by an oxygen plasma treatment [38].

In this paper, we fabricated centimeter-scale single- and bilayer graphene nanomeshes (SGNMs and BGNMs) with various neck width from 8 to 21 nm using BCP self-assembly on CVD-grown graphene. The GNR is more ideal structure for investigating the quantum confinement effect, but the GNM structure was chosen because the nanomesh is quasi-isotropically periodic nano-patterns in a large scale for engaging the quantum confinement and providing directional freedom during the macroscopic measurement and macroscopically interconnected network for higher mechanical stability at suspended geometry. By introducing sub-10 nm patterns into graphene, the quantum confinement can simultaneously and effectively control the electronic and phononic band structures and frequency of phonon scattering, whereas sub-100 nm patterns in graphene only reduce the mean free path of the phonon and rarely affect the band structures and thermopower value. We also investigated the effect of cross-plane coupling in the BGNMs on the thermal and thermoelectric properties. To measure the thermal conductivity of the suspended GNM, we transferred the nanomeshes to micro-sized holey membranes and used the optothermal Raman technique [24,25,39–42]. We also prepared 2-cm-long GNMs on an insulating substrate to measure the thermopower value from the conventional Seebeck coefficient measuring system, carrier concentration and mobility from Hall effect measurements and bandgap from FET characteristic measurements.

2. Experimental

2.1. Graphene synthesis and transfer method

Large-area graphene monolayer sheets were grown using a low-pressure CVD process on Cu foil (25 μm, Alfa Aesar). First, the Cu foil was annealed at 1000 ℃ for 30 min at ~640 mTorr with 100 sccm of H_2 gas flow to increase the grain size and to flatten the surface of the Cu foil. Then, we synthesized a graphene monolayer for 10 min at ~1.2 Torr with 100 and 40 sccm of CH_4 and H_2 at the same temperature. For the cooling process, we rapidly cooled the sample to ambient temperature using the sliding rails of a tube furnace. To transfer the graphene onto a 100 nm SiO_2 deposited Si wafer, poly(methyl methacrylate) (PMMA, Sigma-Aldrich, M_w~350,000) was spin-

coated on the graphene/Cu foil and then transferred by immersing in a 0.5 M ammonium persulfate ((NH_4)$_2S_2O_8$) aqueous solution as a copper etchant and washing with deionized water several times without wrinkles for improved electrical properties of graphene. The PMMA/graphene film was transferred to the substrate, and the PMMA was thoroughly rinsed using acetone. For the bilayer graphene, the transfer process was repeated on the single-layer graphene-transferred substrate.

### 2.2. BCP self-assembly on graphene and fabrication of the GNM

The single and bilayer graphene were treated with a hydroxyl-terminated PMMA homopolymer (M_n~4,000, PDI~1.15, Polymer Source) by spin-coating from 1 wt% chloroform solution, annealing at 170 ℃ for 3 h in vacuum and rinsing with chloroform for avoiding dewetting phenomena of BCP film. PS-b-P2VP ($M_{n,PS}$~50,000, $M_{n,P2VP}$~16,500, PDI~1.09) were purchased from Polymer Source, Inc. A 1 wt% solution of PS-b-P2VP in toluene was spin-coated to form 30-nm-thick films on the graphene. The BCP films were exposed to controlled toluene vapor (0.6 ml of toluene in a 9.3 ml volume glass chamber with a controlled leak) for 1 h and were immersed in ethanol for 30 min at 60 ℃ for the nanostructure reconstruction. The annealed BCP/graphene films were treated with O_2 RIE (90 W, 10 sccm, 10 mTorr) to etch the graphene following solvent annealing. To remove the residual polymer, the nanomesh was thermally treated at 400 ℃ for 1 h in an Ar atmosphere.

2.3. GNM characterization

The morphology of the graphene and BCP films was examined by field emission scanning electron microscopy (FE-SEM, JEOL JSM-6701F) at 10 kV, transmission electron microscopy (TEM, FEI Tecnai G2 F20) at 80 keV, atomic force microscopy (AFM, Asylum Research MFP-3D), and optical microscopy (OM, Nikon Optiphot). Raman spectroscopy (Renishaw inVia) with a 633 nm laser and 100× objective lens was used to analyse the graphene structures. For the sample preparation for TEM and thermal conductivity measurements using the optothermal Raman technique, we transferred the fabricated GNMs to Au-coated silicon nitride membranes with 2.5 μm-diameter holes (Ted Pella, PELCO® holey silicon nitride support film) using a PMMA support layer. The thermopower and electrical conductivity of the GNM or unpatterned graphene films on 2 cm×2 cm SiO_2/Si substrates were measured by a TEP-600 (Seepel Instrument, Korea) thermoelectric measurement instrument in the temperature range from 300 to 520 K under an Ar atmosphere. When we applied temperature differences (0.5, 1.5, and 2.5 ℃ in one direction and −0.5, −1.5, and −2.5 ℃ in the opposite direction) to the two ends of the sample, the probes measured the potential difference and yielded the Seebeck coefficients. The linear correlation coefficients of the linear fit were greater than 0.99. Regarding the confirmation of the instrument reliability, the σ and S of Ni (99.99%) were $1.4 \times 10^7\ S\ m^{-1}$ and $-21.5\ \mu V\ K^{-1}$, respectively. The carrier concentration and mobility were obtained by the Hall effect measurement system (Ecopia, HMS-5500) at a 0.55 T magnetic field and 100 nA electric current with previously prepared thermoelectric samples at room temperature. We also prepared at least 5 GNM samples for each thermopower and electrical conductivities measurement and expressed standard deviation by error bars. The fabrication procedure and characterization of FETs are described in detail in the Supporting information.

3. Results and discussion

Fig. 1 schematically illustrates the GNM fabrication based on the BCP self-assembly and reactive ion etching (RIE) process on CVD-grown graphene sheets. First, graphene monolayer sheets were grown using a low-pressure CVD process on Cu foil at 1000 ℃ with controlled
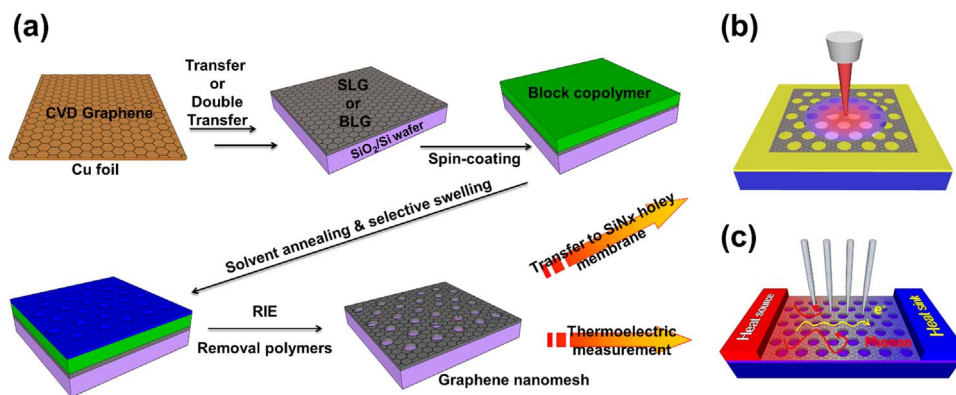
Fig. 1. Fabrication and thermal measurements of a sub-10 nm GNM. (a) Schematic of the fabrication of the sub-10 nm GNMs using BCP self-assembly with RIE on SLG or repeatedly transferred BLG sheets. (b) Schematic image of the optothermal Raman technique for measuring the thermal conductivity of the graphene nanomesh. (c) Schematic of the thermoelectric measurement and transport behavior of electrons and phonons controlled by nanomesh-provided edge scattering.
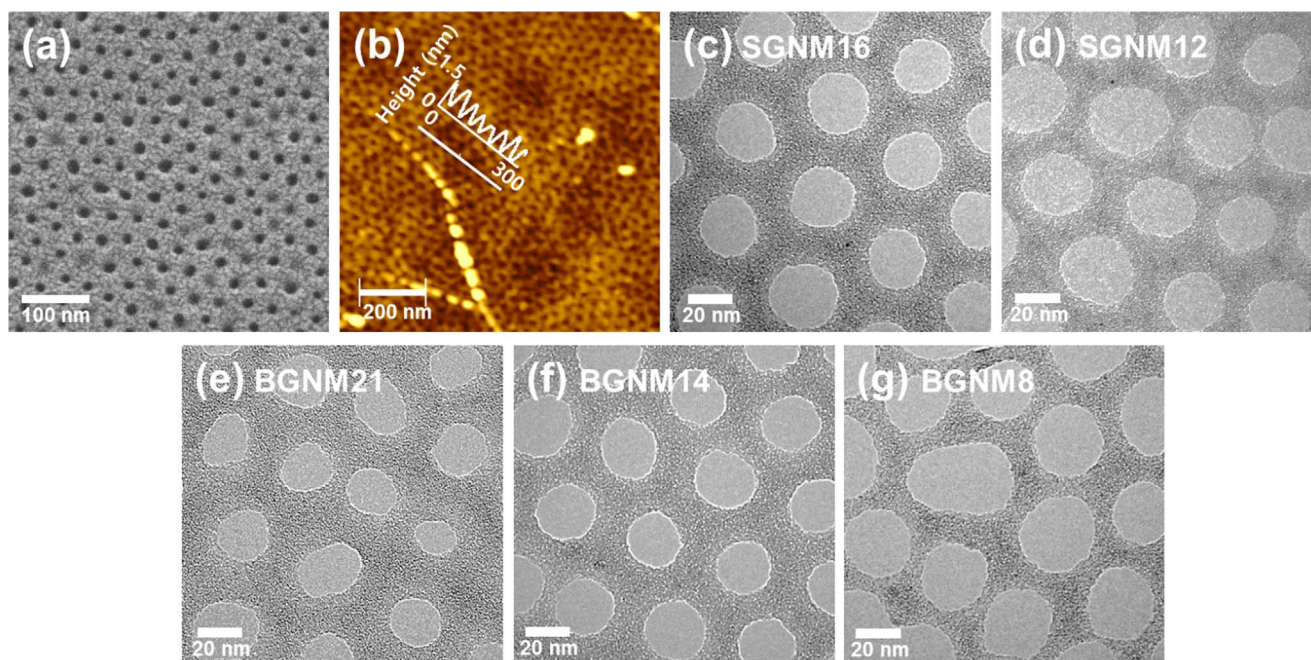

Fig. 2. Structures of the GNM. (a) SEM images of the PS-*b*-P2VP thin films on graphene sheets after solvent annealing with saturated toluene vapor for 1 h and sequential immersion in ethanol for 30 min at 60 °C to swell the spherical P2VP domain selectively and form topographical hexagonal patterns. (b) AFM image of the oxygen RIE process (90 W, 6 sccm, 10 mTorr, 13 s) for the SGNM film. (c-g) TEM images of (c-d) the SGNM films and (e-g) BGNM films after RIE for (c, e) 13 s, (d, f) 18 s, and (g) 23 s to control the neck width of the GNM. SGNM16 denotes the SGNM with a neck width of 16 nm.

H_2 and CH_4 gas flows. The as-synthesized graphene with a supporting poly(methyl methacrylate) (PMMA) layer was transferred to a SiO_2-deposited Si wafer and rinsed with acetone to remove residual polymers; then, an optional second graphene sheet was repeatedly transferred onto the first graphene/SiO_2/Si substrate for BLG. Fig. S1 in the Supporting information shows the morphology and Raman spectra of the double-transferred graphene sheets on the SiO_2/Si wafer, which corresponded well with the properties of BLG [43–45]. On the transferred SLGs or BLGs, 66.5 kg mol^{-1} of PS-*b*-P2VP (76.7 vol% of PS) was spin-coated and solvent-annealed with slightly PS selective toluene vapor in 1 h to form hexagonally packed spherical nanostructures [46]. To develop topographical hole patterns of BCPs, P2VP spherical domains were selectively swelled by immersing in ethanol at 60 °C for 30 min [47]; 42 nm period hole patterns can be seen in the SEM image of Fig. 2a. We then etched the exposed nanohole area of graphene using an O_2 RIE process (90 W, 10 mTorr, 10 sccm). Rinsing in toluene and thermal treatment at 400 °C for 1 h in an Ar atmosphere was performed to remove the residuals from the samples. For transmission electron microscopy (TEM) analysis and thermal con-

ductivity measurement using the optothermal Raman technique (Fig. 1b) we additionally transferred the fabricated GNMs or graphenes to Au-coated silicon nitride (SiN_x) membranes with 2.5-µm-diameter holes using a PMMA support layer. Other measurements including the Seebeck coefficients and FETs were carried out with supported geometry on a SiO_2/Si substrate (Fig. 1c).

In the AFM image of SGNM in Fig. 2b, hexagonally holed GNM structures were fully developed in a large area of the films without impurities, and the height difference between the mesh and holes was approximately 1 nm, which is comparable to monolayer graphene in the AFM experiments [38]. We controlled the neck width of graphene nanomesh patterns by varying the etching time from 8 to 23 s. Transmission electron microscopy (TEM) studies were then carried out for precise characterization of the GNM nanostructures. Fig. 2c-g show the TEM images of SGNMs (c, d) and BGNMs (e-g) with variable neck widths. They clearly exhibit hexagonally arranged and circular-shaped nanoholes. The SGNM samples with an etching time of 13 and 18 s exhibit the averaged neck width of 16.3 nm and 12.2 nm, respectively. The BGNMs with 13 s, 18 s and 23 s of etching time show
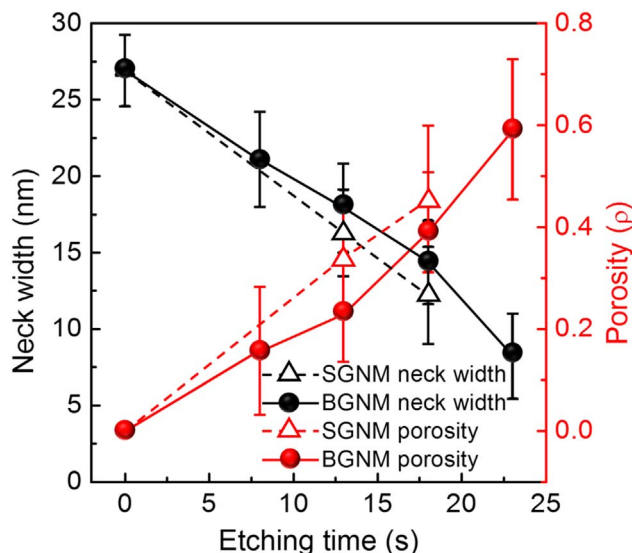
Fig. 3. Neck width and porosity of the GNMs. Neck width and porosity of the SGNMs and BGNMs as a function of RIE time from the image analysis. As increasing RIE etching time, the neck widths of the GNMs are getting decrease and the porosity of the GNMs gradually increase owing to imperfect anisotropic etching of RIE process.

their average neck width of 21.1 nm, 14.4 nm and 8.2 nm, respectively. For the simplicity we hereafter denote the samples as SGNM16, SGNM12, BGNM21, BGNM14 and BGNM8 as their neck widths. The statistical analysis of the neck width and porosity of SGNMs and BGNMs are conducted and the results are shown in Fig. 3 and distribution diagrams are shown in Fig. S2. The standard deviations of variously etched neck widths, which is exhibited by error bars, are relatively narrow (approximately 2 nm) and can represent the ensemble average thermal and thermoelectric properties of graphene nanomeshes within endurable irregularity. The neck widths of the BGNMs were slightly thicker than those of the SGNMs at the same etching time because of the additional etching time required to punch the additional graphene layer of the BLG. We could not produce GNMs with smaller neck width because upon further etching time longer than 18 s for SGNMs and 23 s for BGNM the some of the holes start to merge and the GNMs are mechanically too weak to proceed the transfer process to the SiNx membrane. We also estimated the porosity of the GNMs, the relative area of holes to the total area ($\rho = A_h/A_{tot}$) of the sample, by an image analysis and it significantly increases from ~16% for BGNM21 to ~59% for BGNM8. The coverage of graphene in nanomesh (1−ρ) is necessary for the calculation of thermal conductivity.

To verify the chemical condition of the suspended GNM structures as well as to compare with that of the starting materials of SLG and BLG, Raman spectroscopy was performed under 633 nm He-Ne laser light excitation, as shown in Fig. 4. For both the SGNMs and the BGNMs, the Raman G and 2D peaks maintain their shape and sharpness although their intensities are slightly lowered compare to those for the pristine samples. This suggests that the sp² structures still remain at the basal plain after the etching process. The intensities of D and D′ peaks increase with increasing the etching time, which is attributed to the fact that the total length of the disordered edge increases as the holes are enlarged [48]. Fig. 4c shows a Raman mapping image of successfully transferred graphene & GNMs and fully covered to Au-coated SiN$_x$ holey membrane with 2.5 μm holes.

This Raman spectroscopy can also be used to measure the thermal conductivity of 2D materials. Unlike the conventional measuring method based on micro-fabricated electrical heater/thermometer [26,49,50], the optothermal Raman technique [25,39–41] can be obtained the thermal conductivity of suspended 2D materials using a Raman laser as a heat source and using a characteristic that the Raman peak shift changes linearly with temperature. The laser light focused on

the suspended GNMs at the center of a membrane hole acts as a heating source and the heat flows through the sample to the heat sink, the Au-coated membrane. By varying laser power, one can change the temperature of the sample at the laser-irradiated point and the temperature is estimated by the Raman 2D peak position using a pre-calibrated temperature-2D peak position chart and linear regression. The calibration data is shown in Fig. 5a. For the calibration, we used a low laser power of 0.05 mW to avoid the laser heating. The slopes of the 2D peak position versus temperature were −0.064 cm^{-1} K^{-1}, −0.034 cm^{-1} K^{-1}, −0.050 cm^{-1} K^{-1}, and −0.028 cm^{-1} K^{-1} for the SLG, BLG, SGNM and BGNM, respectively. The obtained coefficients are similar to the values for SLG and BLG reported in a previous study [51]. After the calibration, the 2D peak position is used as a measure of local sample temperature. Fig. 5b shows the 2D peak position as a function of the incident laser power. Thermal conductivity can be calculated by a heat-diffusion equation in cylindrical coordinates using the local temperature measured by Raman 2D peak shift and the absorbed laser power [25,39].

The absorbed laser power of pristine graphene Q could be obtained from the difference between the power measured by power meter at an empty hole and that of a graphene-covered hole. The optical absorption of SLG and BLG were measured 2.9 ± 1.0% and 5.7 ± 1.6% at 633 nm wavelength, respectively. The absorbed laser power of GNMs, which were also measured by power meter, have linear correlation with graphene coverage (1-ρ) and can be expressed as Q(1-ρ). In order to calculate the thermal conductivity, we used the heat diffusion equation in cylindrical coordinates from the previous research [25]. The thermal conductivity k of the graphene or GNMs can be described as

$$k = \frac{\alpha \times \ln\left(\frac{R}{r_0}\right)}{2\pi t \left[(T_m - T_0)/(Q - Q_{air})(1-\rho)\right]} \tag{1}$$

where R is the radius of the holes of 1.25 μm; r_0 is the radius of the laser beam of 0.27 μm from the by knife-edge method [39]; t is the thickness of the graphenes or GNMs; α is 0.98 for the 100× objective lens; T_m is the measured temperature; T_0 is the room temperature; ρ is the areal porosity of GNMs which was measured by TEM and averaged in Fig. 3; Q_{air} is the heat loss in air as

$$Q_{air} = \int_{r_0}^{R} 2\pi g \left(T(r) - T_0\right) r dr + \pi r_0^2 g (T_m - T_0) \tag{2}$$

and temperature profile T(r) can be simply adopted from the literature about two-laser Raman thermometry with actual measurement of temperature distribution from the laser [41],

$$T(r) - T_0 = -\frac{\ln\left(\frac{r}{R}\right)}{\ln\left(\frac{R}{r_0}\right)} (T_m - T_0). \tag{3}$$

in this system, the heat transfer coefficient g was set as 2.9×10⁴ W m^{-2} K^{-1} [25].

Measured thermal conductivity as a function of temperature from the Raman peak shift of the SLG, BLG, SGNM and BGNM is plotted in Fig. 5c and d. At 305 K, the thermal conductivity of pristine SLG and BLG were approximately 3170 ± 1280 W m^{-1} K^{-1} and 1650 ± 197 W m^{-1} K^{-1}, respectively. As temperature increases, the thermal conductivity of the pristine samples gradually decreases to ~910 W m^{-1} K^{-1} for SLG and ~550 W m^{-1} K^{-1} for BLG, respectively, which are the representative temperature dependency ($k \sim T^{-1}$) of intrinsic phonon-phonon Umklapp scattering and are consistent with previous results [25,39,40]. The thermal conductivity of the BLG was lower than that of the SLG because of interlayer phonon scattering [51,52]. For all the graphene nanomesh samples, thermal conductivity was much lower than that of the unpatterned graphenes, < 500 W m^{-1} K^{-1} in the measured temperature range. With decreases in the neck width of the GNMs, the thermal conductivities gradually
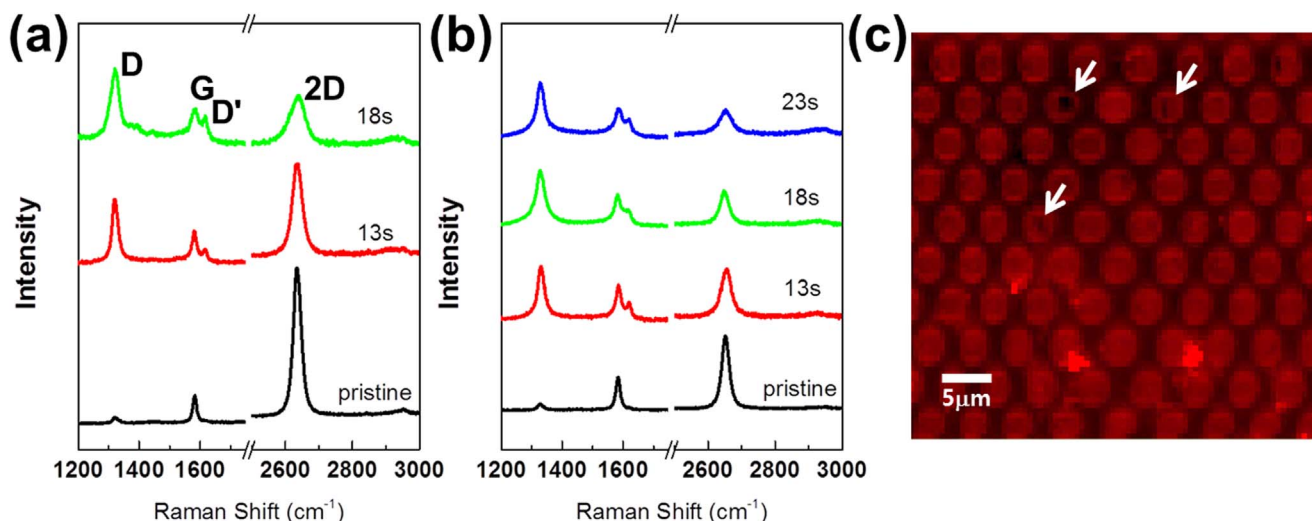
Fig. 4. Raman spectra and mapping image of the GNMs. Raman spectra of suspended (a) SGNM and (b) BGNM upon increasing RIE time. D peak has significantly increased after RIE treatment, and D′ peak is shown for each Raman spectra of GNMs. (c) 100 μm ×100 μm Raman map (2600–2700 cm^{-1}) of the 2D peaks of suspended BGNM on SiN$_x$ holey membrane. The arrows indicate defects of BGNM such as wrinkles or holes.
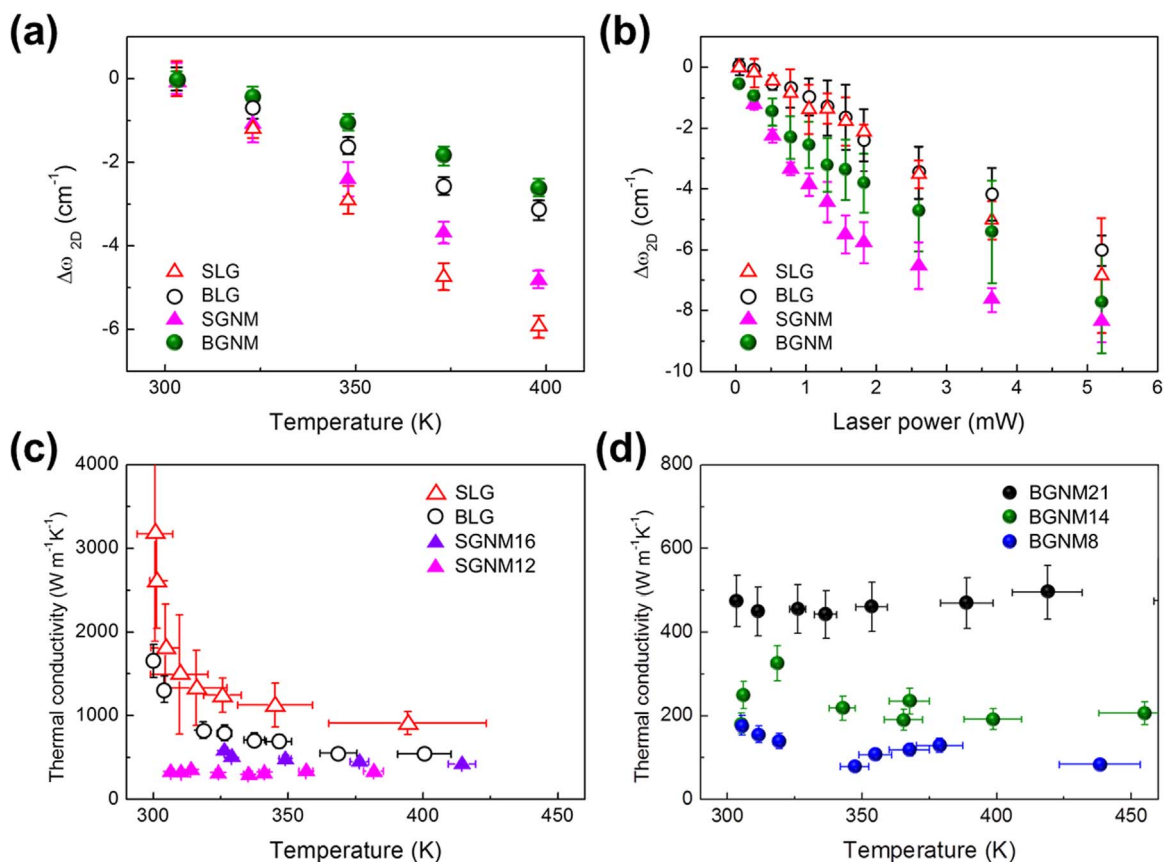

Fig. 5. Thermal conductivity of the suspended SLG, BLG, SGNM and BGNM using an optothermal Raman technique. (a) Raman 2D peak shifts of graphene and graphene nanomeshes as a function of the substrate temperature for use as a thermometer. (b) Raman 2D peak shifts of suspended graphene and GNMs as a function of the laser power for measuring the thermal conductivity. (c) Measured thermal conductivity of pristine SLG, BLG, SGNM16 and SGNM12 as a function of temperature. (d) Thermal conductivity of BGNMs with different neck widths of GNMs, BGNM21, BGNM14 and BGNM8.

decreased from ~579 ± 42 W m^{-1} K^{-1} for SGNM16 to ~337 ± 26 W m^{-1} K^{-1} for SGNM12 in the SGNM sample sets and from ~440 ± 59 W m^{-1} K^{-1} (BGNM21) and ~220 ± 28 W m^{-1} K^{-1} (BGNM14) to ~78 ± 10 W m^{-1} K^{-1} (BGNM8) near 350 K in the BGNM samples. Our sub-20 nm GNMs show relatively very low temperature dependence of thermal conductivities from 300 to 450 K.

Naturally, thermal conductivity reduction is conventionally ob-served from the solid material of porous structures, which derived by Eucken for the thermal conductivity of cylindrical porous solids, $\kappa_{porous}=\kappa_{solid}(1-\varphi)/(1+2\varphi/3)$ [53,54]. The ratio of porous thermal conductivity to solid thermal conductivity are 0.537 for SGNM16, 0.229 for SGNM12, 0.39 for BGNM14 and 0.181 for BGNM8, respectively. Because the classic Eucken model is only valid when the material dimensions are much larger than the phonon MFP, extrinsic
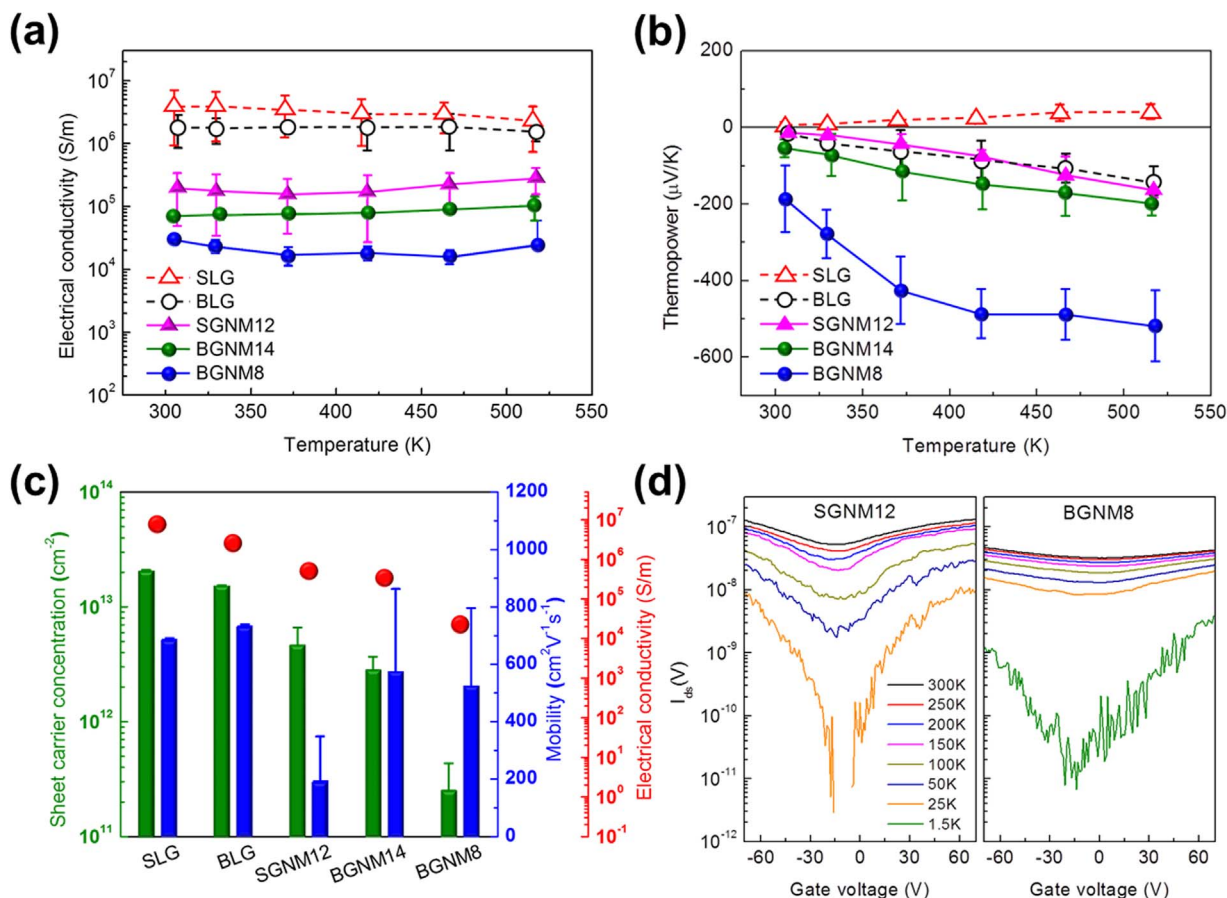
Fig. 6. Electric and thermoelectric properties of graphenes and GNMs. (a) Thermopower values and (b) electrical conductivities as a function of temperature from 300 K to 520 K measured by the conventional Seebeck coefficient measurement system. (c) Electrical conductivity, sheet carrier concentration and mobility measured from the Hall effect measurement of SLG, BLG, SGNM12, BGNM14 and BGNM8 at room temperature. (d) I_{DS}-V_G transfer curves of the SGNM12 and BGNM8 FETs recorded at V_{DS}=100 mV in the temperature range of 1.5−300 K.

phonon-edge scattering from the mesh-edges and phonon spectrum change from phonon confinement lead to a significant thermal conductivity decrease of our sub-20 nm neck-width GNMs and dramatic discrepancy to the Eucken model. Especially in sub-20 nm nanomesh structure, the phonon energy spectra can be quantized due to the confinement of acoustic phonons which usually decrease phonon group velocity [55]. For the phonon-boundary scattering, the mean free path (MFP) can be described as Λ=D(1+p)/(1-p), where D is the nanostructure size and p is a probability of scattering at the boundary. The parameter p is related to the RMS edge roughness Λ, angle θ_E between the phonon wave vector and the normal to the edge (zig-zag edges for 30° and armchair edges for 0°) and phonon momentum q through p(q)=exp(−4q²·Λ²·cos²θ_E) [56]. Therefore, the phonon-boundary scattering occurs more as the width of the pattern is narrower, the edge roughness is larger, and the edge chirality is closer to the armchair. Because the edges created by O_2 plasma etching are significantly rough which the width of disordered area is approximately 2 nm [57], the pattern width D dominantly regulates the phonon MFP equivalently. The phonon MFP in pristine graphene was estimated up to ~800 nm at RT [58] while our nanomesh neck-widths D are in the range from 8 nm to 20 nm and the GNMs inevitably have complex configuration of edges. Therefore, phonon MFP of GNMs can be considerably reduced to comparable dimension of GNM nanostructures. Relatively, electron MFP of pristine graphene is approximately ~20 nm [26], thus, edge disorder can successfully affects thermal transport more strongly than charge transport in our sub-20 nm GNMs. Also, because the extrinsic geometrical scattering including phonon edge scattering is rarely correlated with temperature [21,22], less temperature dependence of thermal conductivities of our GNMs

are under control of edge phonon scattering regime.

Comparing similar neck widths of SGNMs and BGNMs, such as SGNM12 and BGNM14, the thermal conductivity of BGNM14 is still slightly lower than that of SGNM12, which originates from the additional interlayer phonon scattering or existence of residuals in between two basal plains of BGNMs. Note that the thermal conductivity value for BGNM8 (~78 W m⁻¹ K⁻¹) the lowest thermal conductivity among the suspended graphene structures ever reported. This could be achieved dominantly by the edge phonon scattering and modification of phonon dispersion from the sub-10 nm neck width of the nanomesh structure and additionally by interlayer phonon scattering from the bilayer structure.

The temperature-dependent thermopower and electrical conductivity of 2 cm×2 cm-sized graphene and GNMs on the SiO_x/Si substrate were measured by conventional thin film-type thermoelectric measurement systems, as shown in Fig. 6a and b. As the temperature increases from 300 to 520 K, the Seebeck coefficient gradually increases from 5 ± 2 μV K⁻¹ to 41 ± 17 μV K⁻¹ for SLG and from −22 ± 20 μV K⁻¹ to −120 ± 21 μV K⁻¹ for BLG, which exhibit an agreement with the semiclassical Mott relation [59]. The sign indicates the p-type and n-type characteristics, for the SLG and BLG, and it may be originated from different doping conditions from different geometries of ambipolar 2D materials. The electrical conductivity of pristine SLG was in the range of ~4×10⁶ S m⁻¹ and was slightly higher than that of BLG (~2×10⁶ S m⁻¹). The higher absolute value of the thermopower and the lower electrical conductivity of the BLG compared with the SLG is comparable with previous results [23,38]. The difference may result from the one-side (less) surface/substrate doping at each layer of the BLG compared with both-side doping at the SLG.

For the GNMs, the thermopower of SGNM12 gradually increased from -12 ± 5 μV K^{-1} to -150 ± 27 μV K^{-1} at the same temperature range, and the electrical conductivity decreased to ~2×10^5 S m^{-1} which difference is approximately 1 order of magnitude. For the BGNMs, the wider neck width of BGNM14 exhibited higher thermopower from -54 ± 23 μV K^{-1} to -200 ± 30 μV K^{-1} and less electrical conductivity (~8×10^4 S m^{-1}) compared with that of SGNM12. Further decreasing the neck width of the BGNMs to 8 nm (BGNM8), the thermopower was considerably higher (-190 ± 80 μV K^{-1} at 300 K and -520 ± 92 μV K^{-1} at 520 K), which has not been demonstrated before in carbon-based nano-materials, with decreasing electrical conductivity to ~2×10^4 S m^{-1}. While the graphene edges from oxygen plasma usually bring the p-type doping by oxygen dangling bonds [57], our all GNMs showed n-type characteristics. The graphene shows ambipolar transport in FETs, and the major carrier and their concentration was dominantly affected by the doping from the chemical condition of top surface and bottom substrate, and dangling bonds at the edge of the graphene [60]. Therefore, we optimized the temperature of thermal treatment at 400 °C in Ar atmosphere to minimize the effect of surface/substrate doping and dangling bonds at the edges.

Carrier concentration and mobility, which were obtained using the Hall effect measurement, are also important parameters for interpreting the thermoelectric properties (Fig. 6c). The carrier concentration and mobility behaviors of the SGNMs were quite different with those of the BGNMs. While the mesh structure in the SGNMs relatively lowered the mobility from ~700 cm^2 V^{-1} s^{-1} to ~200 cm^2 V^{-1} s^{-1} and less reduced the carrier concentration from ~2×10^{13} cm^{-2} to ~5×10^{12} cm^{-2}, that of the BGNMs fairly conserved the mobility (slightly changed from ~730 to ~530 cm^2 V^{-1} s^{-1}) and significantly reduced the carrier concentrations from ~1.6×10^{13} cm^{-2} to ~2.2×10^{11} cm^{-2}, at the rate of ~1/70 (BGNM8). The significant reduction of the carrier concentration was related to the decreasing basal plain area of the porous GNM structures and severely confined geometry from the narrower neck width. Because the Seebeck coefficient is inversely proportional to the carrier concentration and proportional to temperature for high carrier concentrations [21–23,61], dramatic decrease of the carrier concentration of the BGNM8 could influence the high thermopower values and high temperature dependency of thermopower.

In order to estimate the effective bandgap of the samples and to investigate its effect on thermoelectric properties, we fabricated GNM FETs on top of a highly doped Si substrate with a 300 nm thick thermally grown SiO$_2$ using electron beam lithography and O$_2$ plasma patterning. The fabrication details are described in Supporting information. Source drain current (I$_{DS}$) was measured with an application of a constant source-drain bias voltage (V$_{DS}$) of 1 mV as a function of back-gate voltage (V$_G$). Fig. 6d shows the representative IDS-VDS curves measured for a GNM-FET at various temperatures. The bandgap of the sample is estimated by the Arrhenius plot as shown in the Fig. S3, using the formula of I$_{DS}$=I$_{DS,0}$.exp[E$_g$/($2k_B$T)]. Here, E$_g$ is the energy bandgap and k_B is the Boltzmann constant. The measured bandgap of SGNM12 was ~60 meV, which is comparable with previous results [16], whereas the bandgap of the narrower neck-width BGNM8 was ~25 meV, considerably lower than that of the SGNMs. This smaller bandgap of BGNMs can be attributed to the interlayer interaction induced parabolic band which leads to larger carrier dispersion near zero energy than the Dirac cones for SGNM. Because the bandgap in graphene has an inverse relationship with carrier mobility [62], we attributed that our BGNM structures avoid significant loss of mobility for maintaining electrical conductivity, effectively reduce the carrier concentration for increasing Seebeck coefficient. Based on these thermoelectric measurements, we achieved a power factor (S$^2\sigma$) of BGNM8 up to ~8200 μW m^{-1} K^{-2} at 520 K due to relatively maintained electrical conductivity and superior thermopower.

Using classical and quantum mechanical calculations, we investigated the effect of both sub-10 nm patterns and cross-plane coupling on thermal conductivity and thermoelectric properties of graphene nanomeshes. The thermal conductivity (κ) calculations of 42 nm pattern period of GNMs with different coverages were performed using molecular dynamics simulations [34,63–65], and our computed κ values are shown in Fig. 7a. The significant reduction in κ for GNM samples is due to the presence of circular edges in nanomesh structure, inducing strong phonon scattering at this edge disorders. With decreasing coverage of GNMs, κ reduces further due to the narrower neck width of the nanomesh structure. Because of the dominant edge-phonon scattering of GNMs, interlayer phonon scattering from the BGNM was relatively less affected to the reduction of thermal conductivity. Our calculated thermal conductivity is on the similar order of magnitude of the experimentally measured value of graphene. For estimations of the electron transport in the GNMs, we employed ab initio electronic structure calculations and the Boltzmann transport approach [66–68]. Based on our computed configuration and band structures of GNMs in Fig. S4, the band gap of BGNM is smaller than that of SGNM at the same coverage of GNMs. Fig. 7b shows our calculated thermopower values as a function of temperature for SGNM and BGNM samples with different coverage. Here, the thermopower values of each sample are obtained at intrinsic carrier concentration of corresponding experimental GNM samples. The coverage of graphene in nanomesh is directly proportional to the carrier concentration, thus, the less coverage GNM has a larger thermopower value. These results
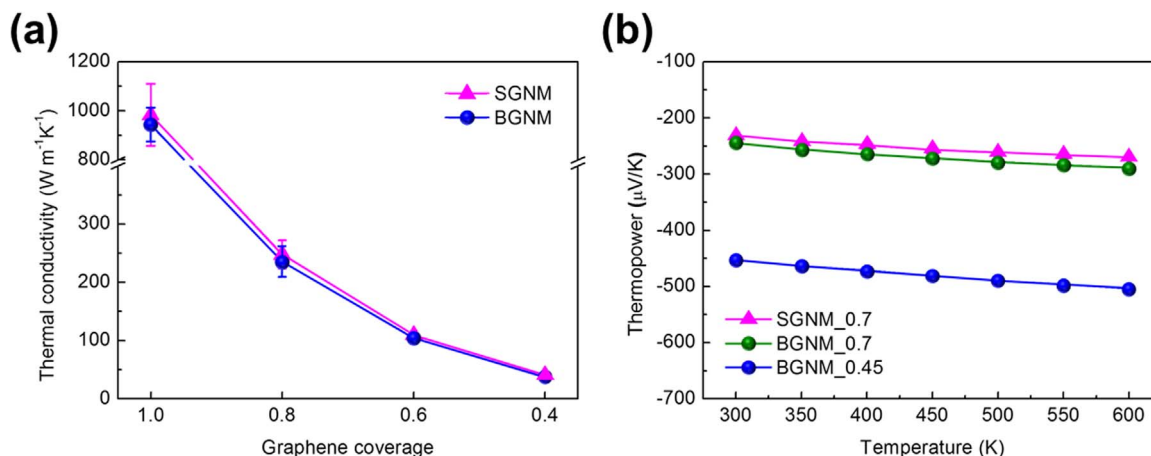

Fig. 7. Theoretical prediction of thermal conductivity and thermoelectric properties of graphenes and GNMs. (a) Thermal conductivity calculations of different coverages of 42 nm period SGNMs and BGNMs from molecular dynamics simulations. (b) Calculated thermopower values of SGNM and BGNMs with different coverage (0.7 and 0.45) as a function of temperature from 300 K to 600 K from *ab initio* electronic structure calculations and the Boltzmann transport approach.

suggest that quantum confinement from a narrower neck width and less bandgap from the bilayer structure led to better thermoelectric efficiency.

4. Conclusions

In conclusion, we fabricated large-sized SGNMs and BGNMs with 8-nm neck widths using BCP self-assembly and firstly measured the thermal conductivity of nano-patterned graphene with unsupported geometry using the optothermal Raman technique and also firstly obtained the thermoelectric properties of nano-patterned graphene. From our measurements, we achieved significantly reduced thermal conductivity of ~78 W m^{-1} K^{-1} from the BGNM with 8 nm neck-width, which is the lowest thermal conductivity of graphene nanostructures, and a maximum thermopower of −520 μV K^{-1} while maintaining their high carrier mobility. Our GNM nanostructures successfully induced dominant phonon-edge scattering within sub-10 nm neck-width scale and quantum confinement for the control of electron and phonon transport behaviors. Because BCP lithography provides a robust fabrication route for forming sub-10 nm nanomesh structure over large areas, our approach can be an excellent platform to investigate the nano-pattern effect or pattern geometry effect on thermal and thermoelectric phenomena of nano-patterned 2D materials including graphene, MoS$_2$ or other thermoelectric materials such as Bi$_2$Te$_3$. In addition, for the flexible thermoelectric materials based on graphene and CNTs, by controlling the physical properties based on the unit material, it can be possible to acquire in-depth understanding of thermoelectric properties of carbon materials and maximize the thermoelectric properties. Therefore, the nano-patterned 2D materials can be expected to contribute for obtaining highly efficient and flexible thermoelectric materials for the self-powered devices of wearable electronics.

Acknowledgements

Appendix A. Supplementary material

Supplementary data associated with this article can be found in the online version at doi:10.1016/j.nanoen.2017.03.019.

References

[1] A.K. Geim, Graphene: status and prospects, Science 324 (2009) 1530–1534. http://dx.doi.org/10.1126/science.1158877.

[2] J.S. Burgess, B.R. Matis, J.T. Robinson, F.A. Bulat, F. Keith Perkins, B.H. Houston, J.W. Baldwin, Tuning the electronic properties of graphene by hydrogenation in a plasma enhanced chemical vapor deposition reactor, Carbon 49 (2011) 4420–4426. http://dx.doi.org/10.1016/j.carbon.2011.06.034.

[3] S. Zhou, D. Siegel, A. Fedorov, A. Lanzara, Metal to insulator transition in epitaxial graphene induced by molecular doping, Phys. Rev. Lett. 101 (2008) 86402. http://dx.doi.org/10.1103/PhysRevLett.101.086402.

[4] M. Han, B. Özyilmaz, Y. Zhang, P. Kim, Energy band-gap engineering of graphene nanoribbons, Phys. Rev. Lett. 98 (2007) 206805. http://dx.doi.org/10.1103/PhysRevLett.98.206805.

[5] Z. Chen, Y.-M. Lin, M.J. Rooks, P. Avouris, Graphene nano-ribbon electronics, Physica E 40 (2007) 228–232. http://dx.doi.org/10.1016/j.physe.2007.06.020.

[6] K. Nakada, M. Fujita, G. Dresselhaus, M. Dresselhaus, Edge state in graphene ribbons: nanometer size effect and edge shape dependence, Phys. Rev. B 54 (1996)

[7] X. Li, X. Wang, L. Zhang, S. Lee, H. Dai, Chemically derived, ultrasmooth graphene nanoribbon semiconductors, Science 319 (2008) 1229–1232. http://dx.doi.org/10.1126/science.1150878.

[8] L. Jiao, L. Zhang, X. Wang, G. Diankov, H. Dai, Narrow graphene nanoribbons from carbon nanotubes, Nature 458 (2009) 877–880. http://dx.doi.org/10.1038/nature07919.

[9] J. Bai, X. Duan, Y. Huang, Rational fabrication of graphene nanoribbons using a nanowire etch mask, Nano Lett. 9 (2009) 2083–2087.

[10] W.J. Yu, X. Duan, Tunable transport gap in narrow bilayer graphene nanoribbons, Sci. Rep. 3 (2013) 1248. http://dx.doi.org/10.1038/srep01248.

[11] D.S. Lee, C. Riedl, T. Beringer, A.H. Castro Neto, K. von Klitzing, U. Starke, J.H. Smet, Quantum Hall effect in twisted bilayer graphene, Phys. Rev. Lett. 107 (2011) 216602. http://dx.doi.org/10.1103/PhysRevLett.107.216602.

[12] International Technology Roadmap for Semiconductors, ITRS 2011 Edition, 2011. ⟨http://www.itrs.net/Links/2011ITRS/2011Chapters/2011ERM.pdf⟩.

[13] F.S. Bates, G.H. Fredrickson, Block copolymer thermodynamics: theory and experiment, Annu. Rev. Phys. Chem. 41 (1990) 525–557. http://dx.doi.org/10.1146/annurev.pc.41.100190.002521.

[14] M. Park, C. Harrison, P.M. Chaikin, R.A. Register, D.H. Adamson, Block copolymer lithography: periodic arrays of ~10^{11} holes in 1 square centimeter, Science 276 (1997) 1401–1404. http://dx.doi.org/10.1126/science.276.5317.1401.

[15] J. Bai, X. Zhong, S. Jiang, Y. Huang, X. Duan, Graphene nanomesh, Nat. Nanotechnol. 5 (2010) 190–194. http://dx.doi.org/10.1038/nnano.2010.8.

[16] X. Liang, Y.-S. Jung, S. Wu, A. Ismach, D.L. Olynick, S. Cabrini, J. Bokor, Formation of bandgap and subbands in graphene nanomeshes with sub-10 nm ribbon width fabricated via nanoimprint lithography, Nano Lett. 10 (2010) 2454–2460. http://dx.doi.org/10.1021/nl100750v.

[17] M. Kim, N.S. Safron, E. Han, M.S. Arnold, P. Gopalan, Fabrication and characterization of large-area, semiconducting nanoperforated graphene materials, Nano Lett. 10 (2010) 1125–1131. http://dx.doi.org/10.1021/nl9032318.

[18] G. Liu, Y. Wu, Y.-M. Lin, D.B. Farmer, J.A. Ott, J. Bruley, A. Grill, P. Avouris, D. Pfeiffer, A.A. Balandin, C. Dimitrakopoulos, Epitaxial graphene nanoribbon array fabrication using BCP-assisted nanolithography, ACS Nano. 6 (2012) 6786–6792. http://dx.doi.org/10.1021/nn301515a.

[19] X. Liang, S. Wi, Transport characteristics of multichannel transistors made from densely aligned Sub-10 nm half-pitch graphene nanoribbons, ACS Nano 6 (2012) 9700–9710.

[20] J.G. Son, M. Son, K.-J. Moon, B.H. Lee, J.-M. Myoung, M.S. Strano, M.-H. Ham, C.A. Ross, Sub-10 nm graphene nanoribbon array field-effect transistors fabricated by block copolymer lithography, Adv. Mater. 25 (2013) 4723–4728. http://dx.doi.org/10.1002/adma.201300813.

[21] A.A. Balandin, Thermal properties of graphene and nanostructured carbon materials, Nat. Mater. 10 (2011) 569–581. http://dx.doi.org/10.1038/nmat3064.

[22] Y. Xu, Z. Li, W. Duan, Thermal and thermoelectric properties of graphene, Small 10 (2014) 2182–2199. http://dx.doi.org/10.1002/smll.201303701.

[23] P. Dollfus, V. Hung Nguyen, J. Saint-Martin, Thermoelectric effects in graphene nanostructures, J. Phys. Condens. Matter 27 (2015) 133204. http://dx.doi.org/10.1088/0953-8984/27/13/133204.

[24] A.A. Balandin, S. Ghosh, W. Bao, I. Calizo, D. Teweldebrhan, F. Miao, C.N. Lau, Superior thermal conductivity of single-layer graphene, Nano Lett. 8 (2008) 902–907. http://dx.doi.org/10.1021/nl0731872.

[25] S. Chen, Q. Wu, C. Mishra, J. Kang, H. Zhang, K. Cho, W. Cai, A.A. Balandin, R.S. Ruoff, Thermal conductivity of isotopically modified graphene, Nat. Mater. 11 (2012) 203–207. http://dx.doi.org/10.1038/nmat3207.

[26] M.-H. Bae, Z. Li, Z. Aksamija, P.N. Martin, F. Xiong, Z.-Y. Ong, I. Knezevic, E. Pop, Ballistic to diffusive crossover of heat flow in graphene ribbons, Nat. Commun. 4 (2013) 1734. http://dx.doi.org/10.1038/ncomms2755.

[27] Y. Ouyang, J. Guo, A theoretical study on thermoelectric properties of graphene nanoribbons, Appl. Phys. Lett. 94 (2009) 263107. http://dx.doi.org/10.1063/1.3171933.

[28] H. Sevinçli, G. Cuniberti, Enhanced thermoelectric figure of merit in edge-disordered zigzag graphene nanoribbons, Phys. Rev. B 81 (2010) 113401. http://dx.doi.org/10.1103/PhysRevB.81.113401.

[29] Y. Chen, T. Jayasekera, A. Calzolari, K.W. Kim, M.B. Nardelli, Thermoelectric properties of graphene nanoribbons, junctions and superlattices, J. Phys. Condens. Matter 22 (2010) 372202. http://dx.doi.org/10.1088/0953-8984/22/37/372202.

[30] F. Mazzamuto, V. Hung Nguyen, Y. Apertet, C. Caër, C. Chassat, J. Saint-Martin, P. Dollfus, Enhanced thermoelectric properties in graphene nanoribbons by resonant tunneling of electrons, Phys. Rev. B 83 (2011) 235426. http://dx.doi.org/10.1103/PhysRevB.83.235426.

[31] T. Gunst, T. Markussen, A.-P. Jauho, M. Brandbyge, Thermoelectric properties of finite graphene antidot lattices, Phys. Rev. B 84 (2011) 155449. http://dx.doi.org/10.1103/PhysRevB.84.155449.

[32] H. Karamitaheri, M. Pourfath, M. Pazoki, R. Faez, H. Kosina, Graphene-based antidots for thermoelectric applications, J. Electrochem. Soc. 158 (2011) K213–K216. http://dx.doi.org/10.1149/2.025112jes.

[33] H. Karamitaheri, M. Pourfath, R. Faez, H. Kosina, Geometrical effects on the thermoelectric properties of ballistic graphene antidot lattices, J. Appl. Phys. 110 (2011) 54506. http://dx.doi.org/10.1063/1.3629990.

[34] J.Y. Kim, J.-H. Lee, J.C. Grossman, Thermal transport in functionalized graphene, ACS Nano 6 (2012) 9050–9057.

[35] J.Y. Kim, J.C. Grossman, High-efficiency thermoelectrics with functionalized graphene, Nano Lett. 15 (2015) 2830–2835. http://dx.doi.org/10.1021/nl504257q.

[36] C.-R. Wang, W.-S. Lu, L. Hao, W.-L. Lee, T.-K. Lee, F. Lin, I.-C. Cheng, J.-Z. Chen,

Enhanced thermoelectric power in dual-gated bilayer graphene, Phys. Rev. Lett. 107 (2011) 186602. http://dx.doi.org/10.1103/PhysRevLett.107.186602.

[37] S.-G. Nam, D.-K. Ki, H.-J. Lee, Thermoelectric transport of massive Dirac fermions in bilayer graphene, Phys. Rev. B 82 (2010) 245416. http://dx.doi.org/10.1103/PhysRevB.82.245416.

[38] N. Xiao, X. Dong, L. Song, D. Liu, Y. Tay, S. Wu, L.-J. Li, Y. Zhao, T. Yu, H. Zhang, W. Huang, H.H. Hng, P.M. Ajayan, Q. Yan, Enhanced thermopower of graphene films with oxygen plasma treatment, ACS Nano 5 (2011) 2749–2755. http://dx.doi.org/10.1021/nn2001849.

[39] W. Cai, A.L. Moore, Y. Zhu, X. Li, S. Chen, L. Shi, R.S. Ruoff, Thermal transport in suspended and supported monolayer graphene grown by chemical vapor deposition, Nano Lett. 10 (2010) 1645–1651. http://dx.doi.org/10.1021/nl9041966.

[40] S. Chen, A.L. Moore, W. Cai, J.W. Suk, J. An, C. Mishra, C. Amos, C.W. Magnuson, J. Kang, L. Shi, R.S. Ruoff, Raman measurements of thermal transport in suspended monolayer graphene of variable sizes in vacuum and gaseous environments, ACS Nano 5 (2011) 321–328. http://dx.doi.org/10.1021/nn102915x.

[41] J.S. Reparaz, E. Chavez-Angel, M.R. Wagner, B. Graczykowski, J. Gomis-Bresco, F. Alzina, C.M. Sotomayor Torres, A novel contactless technique for thermal field mapping and thermal conductivity determination: two-laser Raman thermometry, Rev. Sci. Instrum. 85 (2014) 34901. http://dx.doi.org/10.1063/1.4867166.

[42] D.L. Nika, A.A. Balandin, Two-dimensional phonon transport in graphene, J. Phys. Condens. Matter 24 (2012) 233203. http://dx.doi.org/10.1088/0953-8984/24/23/233203.

[43] R.W. Havener, H. Zhuang, L. Brown, R.G. Hennig, J. Park, Angle-resolved raman imaging of interlayer rotations and interactions in twisted bilayer graphene, Nano Lett. 12 (2012) 3162–3167. http://dx.doi.org/10.1021/nl301137k.

[44] K. Kim, S. Coh, L.Z. Tan, W. Regan, J.M. Yuk, E. Chatterjee, M.F. Crommie, M.L. Cohen, S.G. Louie, A. Zettl, Raman spectroscopy study of rotated double-layer graphene: misorientation-angle dependence of electronic structure, Phys. Rev. Lett. 108 (2012) 246103. http://dx.doi.org/10.1103/PhysRevLett.108.246103.

[45] Z. Ni, Y. Wang, T. Yu, Y. You, Z. Shen, Reduction of Fermi velocity in folded graphene observed by resonance Raman spectroscopy, Phys. Rev. B 77 (2008) 235403. http://dx.doi.org/10.1103/PhysRevB.77.235403.

[46] H. Cho, H. Park, T.P. Russell, S. Park, Precise placements of metal nanoparticles from reversible block copolymer nanostructures, J. Mater. Chem. 20 (2010) 5047–5051. http://dx.doi.org/10.1039/C0jm00651c.

[47] J.G. Son, W.K. Bae, H. Kang, P.F. Nealey, K. Char, Placement control of nanomaterial block copolymer thin films, ACS Nano 3 (2009) 3927–3934.

[48] J. Lee, K. Kim, W.I. Park, B.-H. Kim, J.H. Park, T.-H. Kim, S. Bong, C.-H. Kim, G. Chae, M. Jun, Y. Hwang, Y.S. Jung, S. Jeon, Uniform graphene quantum dots patterned from self-assembled silica nanodots, Nano Lett. 12 (2012) 6078–6083. http://dx.doi.org/10.1021/nl302520m.

[49] J.H. Seol, I. Jo, A.L. Moore, L. Lindsay, Z.H. Aitken, M.T. Pettes, X. Li, Z. Yao, R. Huang, D. Broido, N. Mingo, R.S. Ruoff, L. Shi, Two-dimensional phonon transport in supported graphene, Science 328 (2010) 213–216. http://dx.doi.org/10.1126/science.1184014.

[50] M.T. Pettes, I. Jo, Z. Yao, L. Shi, Influence of polymeric residue on the thermal conductivity of suspended bilayer graphene, Nano Lett. 11 (2011) 1195–1200. http://dx.doi.org/10.1021/nl104156y.

[51] H. Li, H. Ying, X. Chen, D.L. Nika, A.I. Cocemasov, W. Cai, A.A. Balandin, S. Chen, Thermal conductivity of twisted bilayer graphene, Nanoscale 6 (2014) 13402–13408. http://dx.doi.org/10.1039/c4nr04455j.

[52] S. Ghosh, W. Bao, D.L. Nika, S. Subrina, E.P. Pokatilov, C.N. Lau, A.A. Balandin, Dimensional crossover of thermal transport in few-layer graphene, Nat. Mater. 9 (2010) 555–558. http://dx.doi.org/10.1038/nmat2753.

[53] P.E. Hopkins, C.M. Reinke, M.F. Su, R.H. Olsson, E.A. Shaner, Z.C. Leseman, J.R. Serrano, L.M. Phinney, I. El-Kady, Reduction in the thermal conductivity of single crystalline silicon by phononic crystal patterning, Nano Lett. 11 (2011) 107–112. http://dx.doi.org/10.1021/nl102918q.

[54] J. Tang, H.T. Wang, D.H. Lee, M. Fardy, Z. Huo, T.P. Russell, P. Yang, Holey silicon as an efficient thermoelectric material, Nano Lett. 10 (2010) 4279–4283. http://dx.doi.org/10.1021/nl102931z.

[55] A. Balandin, K. Wang, Significant decrease of the lattice thermal conductivity due to phonon confinement in a free-standing semiconductor quantum well, Phys. Rev. B 58 (1998) 1544–1549. http://dx.doi.org/10.1103/PhysRevB.58.1544.

[56] Z. Aksamija, I. Knezevic, Lattice thermal conductivity of graphene nanoribbons: anisotropy and edge roughness scattering, Appl. Phys. Lett. 98 (2011) 141919. http://dx.doi.org/10.1063/1.3569721.

[57] M. Kim, N.S. Safron, E. Han, M.S. Arnold, P. Gopalan, Electronic transport and Raman scattering in size- controlled nanoperforated graphene, ACS Nano 6 (2012) 9846–9854.

[58] S. Ghosh, I. Calizo, D. Teweldebrhan, E.P. Pokatilov, D.L. Nika, A.A. Balandin, W. Bao, F. Miao, C.N. Lau, Extremely high thermal conductivity of graphene: prospects for thermal management applications in nanoelectronic circuits, Appl. Phys. Lett. 92 (2008) 151911. http://dx.doi.org/10.1063/1.2907977.

[59] Y.M. Zuev, W. Chang, P. Kim, Thermoelectric and magnetothermoelectric transport measurements of graphene, Phys. Rev. Lett. 102 (2009) 1–4. http://dx.doi.org/10.1103/PhysRevLett.102.096807.

[60] N.D.K. Tu, J. Choi, C.R. Park, H. Kim, Remarkable conversion between n- and p-type reduced graphene oxide on varying the thermal annealing temperature, Chem. Mater. 27 (2015) 7362–7369. http://dx.doi.org/10.1021/acs.chemmater.5b02999.

[61] G.J. Snyder, E.S. Toberer, Complex thermoelectric materials, Nat. Mater. 7 (2008)

105–114 ⟨http://www.ncbi.nlm.nih.gov/pubmed/18219332⟩.

[62] J. Wang, R. Zhao, M. Yang, Z. Liu, Z. Liu, Inverse relationship between carrier mobility and bandgap in graphene, J. Chem. Phys. 138 (2013) 84701. http://dx.doi.org/10.1063/1.4792142.

[63] D.A. Weitz, D.J. Pine, P.N. Pusey, R.J.A. Tough, Nondiffusive Brownian motion studied by diffusing-wave spectroscopy, Phys. Rev. Lett. 63 (1989) 1747–1750. http://dx.doi.org/10.1103/PhysRevLett.63.1747.

[64] S. Viscardy, J. Servantie, P. Gaspard, Transport and Helfand moments in the Lennard-Jones fluid. II. Thermal conductivity, J. Chem. Phys. 126 (2007) 184513. http://dx.doi.org/10.1063/1.2724820.

[65] S. Plimpton, Fast parallel algorithms for short-range molecular dynamics, J. Comput. Phys. 117 (1995) 1–19. http://dx.doi.org/10.1006/jcph.1995.1039.

[66] G. Kresse, J. Furthmüller, Efficient iterative schemes for ab initio total-energy calculations using a plane-wave basis set, Phys. Rev. B 54 (1996) 11169–11186. http://dx.doi.org/10.1103/PhysRevB.54.11169.

[67] G. Kresse, From ultrasoft pseudopotentials to the projector augmented-wave method, Phys. Rev. B 59 (1999) 1758–1775. http://dx.doi.org/10.1103/PhysRevB.59.1758.

[68] J.P. Perdew, Y. Wang, Accurate and simple analytic representation of the electron-gas correlation energy, Phys. Rev. B 45 (1992) 13244–13249. http://dx.doi.org/10.1017/CBO9781107415324.004.

Jinwoo Oh is a Ph.D. candidate in School of Chemistry and Biological Engineering from Seoul National University. He received B.S. and M.S. in Polymer Science and Engineering from Inha University. His research interests include nano-structuring of 2-dimensional materials such as graphene and to control the thermoelectric characteristics and thermal transport of nanopatterned materials.

Hoyeon Yoo received her bachelor degree in Department of Chemistry in Sangmyung University. She then received her master's degree in Department of Chemical and Biological Engineering from Korea University. During her studies, she studied block-copolymer self-assembly for nano structure construction. Her research interests are in the use of block-copolymer for nano patterning technique.

Jaeyoo Choi is a Ph.D. student at Department of Materials Science and Engineering in Seoul National University. He received B.S. and M.S in Biomaterials Science and Engineering from Seoul National University. He is interested in thermoelectric energy conversion and has studied on thermoelectric materials and modules by both experimental and fundamental approaches. Especially, he focused on development of flexible thermoelectric generators based on Nano-carbon materials such as a carbon nanotube, graphene.

Jeong Yun Kim is a Postdoctoral Associates at Massachusetts Institute of Technology Chemical Engineering Department. She received B.S. in Materials Science & Engineering from Seoul National University and Ph.D. in Materials Science & Engineering from Massachusetts Institute of Technology. Her research interests focus on adopting cutting-edge computational approaches to understanding and predicting new materials for advances in energy applications, such as thermoelectrics, catalysis, carbon capture and hydrogen storage.

Dong Su Lee is a Senior Research Scientist at Applied Quantum Composites Research Center in Korea Institute of Science & Technology. He received his B.S., M.S. and Ph.D. degrees in Department of Physics, Seoul National University and worked as a postdoctoral researcher in von Klitzing's department at Max-Planck-Institute for Solid State Research (MPI-FKF). His research interests focus on transport measurement on nanostructures and nano-devices and their quantum phenomena.

Jong Hyuk Park is a Senior Research Scientist at Photo-Electronic Hybrids Research Center in Korea Institute of Science and Technology. He received B.S. and M.S. in School of Chemical and Biological Engineering from Seoul National University. He then received Ph.D. in Chemical Engineering from University of Minnesota. His current research is focused on energy conversion devices.
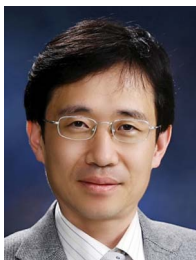
Myung Jong Kim received the B.S degree in chemistry from Yonsei University, Seoul, Korea, in 1998 and the M.S degree in physics from Yonsei University, Seoul, Korea, in 2000, respectively. He received the Ph.D. degree from the Department of Physics and Astronomy, Carbon Nanotechnology Lab, Rice University, under guidance of Prof. Richard E. Smalley. From 2006 to 2008, he worked as a Postdoctoral Fellow at University of Pennsylvania with Prof. Larry Sneddon. From 2008 to 2010, he had worked as senior researcher in Process Development Team, Semiconductor R & D Center, Samsung Electronics. Since 2010, he has been a Senior Research Scientist and Associate Professor of UST, Applied Quantum Composites Research Center, Korea Institute of Science and Technology in Jeonbuk. His research area is "Carbon and boron nitride nanostructure synthesis and their physical properties".

Sang-Soo Lee is a Principal Research Scientist/Head in Photo-Electronic Hybrids Research Center, Korea Institute of Science and Technology, South Korea. He received the BS and MS degrees in Chemical Technology from Seoul National University in 1990 and 1992, respectively, and the Ph.D. degree in Chemical Technology from Seoul National University in 1995. He was a research fellow in Material Science and Engineering in University of Michigan, Ann Arbor, USA from 1995 to 1997. His research focuses on the development of novel materials and devices for electron/ion transport-based interconnection and renewable energy conversion.

Jong-Chan Lee is a professor in School of Chemistry and Biological Engineering from Seoul National University. He received B.S. and M.S. in Chemical Technology from Seoul National University in 1989 and 1992. He then received his Ph.D. degree at Case Western Reserve University in 1998. His research focuses on synthesizing novel polymeric materials for fuel cells, electrolyte, and biocidal polymers.

Heesuk Kim is a Principal Researcher at Photo-electronic Hybrids Research Center in Korea Institute of Science & Technology. She received B.S. in Organic Chemistry from Seoul National University and Ph.D. in Materials Chemistry from University of Wisconsin at Madison. Her research interests focus on design of hybrid materials for electronic and energy (thermoelectric) devices.

Woo Nyon Kim is a professor in Department of Chemical and Biological Engineering from Korea University. He received B.S. in Department of Chemical Engineering from Korea University in 7989. He then received M.S and Ph.D. at University of Waterloo in 1984 and 1987, respectively. His research interests focus on polymer blends and multi-phase polymer system.

Jeong Gon Son is a Senior Research Scientist at Photo-electronic Hybrids Research Center in Korea Institute of Science & Technology. He received B.S. and Ph.D. in Chemical Engineering from Seoul National University and moved to United States for postdoctoral research in Materials Science & Engineering from Massachusetts Institute of Technology. His research interests focus on control of nanostructures based on soft electronic materials (graphene, conducting polymers) via self-assembly for superior energy storage and thermoelectric conversion materials.

Jeffrey C. Grossman is the Morton and Claire Goulder and Family Professor in Environmental Systems, and is faculty in the Department of Materials Science and Engineering at MIT. He received his B.A. in Physics from John Hopkins University in 1991, M.S. and Ph.D. in Physics from University of Illinois at Urbana-Champaign in 1992 and 1996, respectively. He tries to apply a combined computational/experimental approach to outstanding science and technology challenges, with emphasis on gaining a deep understanding and then using that to design new materials for advances in energy conversion, energy storage, and water filtration.